14th International Symposium on Turbulence and Shear Flow Phenomena (TSFP14)
Heidelberg, Germany, July 28–31, 2026

GEOMETRY-INDUCED FLOW SEPARATION OVER SURFACE-MOUNTED TRAPEZOIDAL PROTRUSIONS

Shahar Zuckerman
Faculty of mechanical engineering
Technion- Israel Institute of Technology
Haifa, Israel
Shahar.z@campus.technion.ac.il

Jibu Tom Jose
Faculty of mechanical engineering
Technion- Israel Institute of Technology
Haifa, Israel
jibu.jose@campus.technion.ac.il

Omri Ram
Faculty of mechanical engineering
Technion- Israel Institute of Technology
Haifa, Israel
Omri.ram@technion.ac.il

ABSTRACT

In many engineering systems, surfaces are disrupted by small protrusions such as rivets, sensors, or worn features that act as blunt obstacles to the flow. These elements can trigger flow separation, increase drag, and promote cavitation. This study examines how the geometry of simple two-dimensional surface-mounted protrusions—specifically their length and trailing-edge angle—affects the resulting flow structure. Experiments were conducted in a closed-loop water tunnel at $Re_h = 60{,}000$, using stereo PIV to resolve the velocity field around rectangular obstacles of constant height. The protrusion length is varied ($L^* = 1\,\&\,4$) to investigate the effects on separation, reattachment, and turbulence production. Short obstacles produce a single large recirculation region sustained by return flow from the wake. Increasing the length leads to the formation of a second recirculation zone on the top surface, with peak k observed when these two regions interact. The results also demonstrate that preserving streamwise momentum at the leading edge, through surface curvature, can promote full separation at the trailing edge. These findings provide new insights into flow separation mechanisms over blunt surface features.

1 Introduction

Flow separation induced by abrupt geometric surface non-uniformity has been extensively studied due to its relevance in virtually every engineering flow system. The simplest configuration studied is that in which the flow encounters a sharp 90-degree step, including an inward-protruding forward-facing step (FFS) Graziani *et al.* (2017); Hattori & Nagano (2010); Scheit *et al.* (2013); Larose *et al.* (2025) and a backward-facing step (BFS) forming an abrupt expansion Kostas *et al.* (2002); Yamada & Nakamura (2016); Agarwal *et al.* (2023); Scharnowski *et al.* (2017). A more complex scenario arises when a localised rectangular obstruction creates a FFS followed by a BFS before the flow has fully readjusted to the reduced cross-sectional area. In this case, the length of the obstruction governs the interaction between the leading-edge and trailing-edge separations, giving rise to a variety of flow field topologies Chen *et al.* (2018); van der Kindere & Ganapathisubramani (2018); Schröder *et al.* (2020); Fang *et al.* (2022); Pastoor *et al.* (2008); Sagharichi *et al.* (2023); Agyei-Agyemang *et al.* (2024). The interaction between the free stream and the localised obstruction, and the resulting separated flow, have been shown to significantly influence heat transfer, induced drag, pressure fluctuations, noise production, and energy losses Simpson (1989). Additionally, the high shear rates and frequent vortex shedding induced by wall-mounted obstructions have been shown to promote abrupt phase change, increasing susceptibility to cavitation inception and boiling in thermally active flow systems.

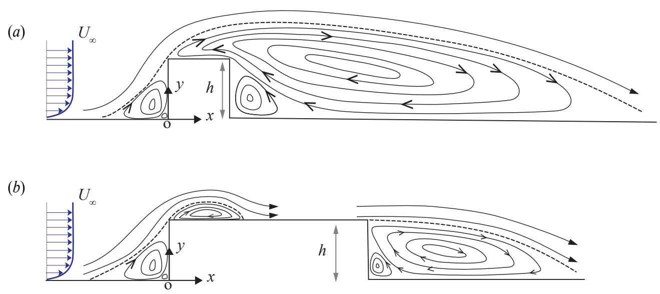

Figure 1. Flow topology associated with a rectangular irregularity across different aspect ratios for (*a*) a continuous unified recirculation region and (*b*) two distinct separation regions.

Figure 1 illustrates schematic mean flow fields around a rectangular wall-mounted two-dimensional obstruction, based on van der Kindere & Ganapathisubramani (2018). The flow around the obstruction is governed by the following parameters: the Reynolds number, $Re = U_\infty h/\nu$, where U_∞, h, and ν are the free-stream velocity, obstruction height, and kinematic viscosity, respectively. For the cases presented in this study, the incoming boundary layer thickness δ_{99} is approximately equal to the obstruction height h. The obstruction geometry is characterised by the aspect ratio $AR = L/h$, where L

is the obstruction length. Figure 1(*a*) depicts the flow around a body with a small aspect ratio obstruction. In this case, the flow forms a single continuous separation region that begins at the leading edge and extends over the obstruction before reattaching far downstream. Here, the return flow along the lower downstream wall continues to flow over the irregularity, directly impinging on the incoming flow. The direct interaction between the incoming free stream and the returning flow increases local adverse pressure gradients behind the separation, forcing the shear layer away from the obstruction surface. The shear layer does not reattach onto the shorter obstruction, resulting in a large separation region whose streamwise extent considerably exceeds the length of the irregularity. Previous studies have measured the reattachment length for short obstructions to be typically in the range of 6–8h, with some cases extending up to $\sim 10h$. A secondary recirculation region forms as the return flow approaches the downstream foot of the irregularity and separates due to the sharp geometric change in surface direction. As the aspect ratio increases within this regime, the shear layer remains continuous; however, with increasing length, the outer flow increasingly conforms to the geometry, and a smaller portion of the returning flow crosses the trailing edge back towards the leading edge. Eventually, the flow reattaches before the end of the obstruction, and a distinct recirculation region forms on the top surface, in addition to the upstream and downstream recirculation regions. The shear layer arriving at the reattachment location carries a notable momentum deficit, and the resulting topology exhibits only a short distance between the two separation regions. This reduced spacing is associated with intensified interactions and enhanced unsteadiness in the vicinity of both the leading-edge and trailing-edge separation zones. For sufficiently large aspect ratios, the recirculation regions become spatially decoupled. The upstream FFS recirculation region becomes independent of the downstream BFS separation, with negligible mutual influence. The wake recirculation is then governed primarily by the momentum and velocity distribution established along the obstacle's upper surface. Intermittent shedding and unsteady fluctuations originate from the trailing-edge separation, while the upstream recirculation remains largely unaffected by downstream events.

Across all obstruction geometries, the separation regions are predominantly governed by the Reynolds number and the incoming boundary layer thickness. However, it has been established that the recirculation region upstream of the irregularity has no significant influence on the separations occurring downstream of it Graziani *et al.* (2017). The sizes of the recirculation regions and the aspect ratios at which transitions between flow patterns occur depend on the Reynolds number and the incoming turbulence intensity. Previous studies typically report that the transition from linked to distinct FFS and BFS circulation regions occurs at $AR \approx 5$ Fang *et al.* (2022), while van der Kindere & Ganapathisubramani (2018) identifies a threshold of approximately $AR \approx 4$.

A narrow shear layer separates the recirculation region from the overlying free stream. This region is bounded in the streamwise direction by the separation and reattachment points, and in the wall-normal direction it is subjected to the interaction between the high-momentum free stream above and the low-momentum recirculation region adjacent to the surface. The velocity difference across this interface induces rotational motion in the fluid within this layer, which, as the flow translates downstream, accumulates angular momentum and ultimately leads to the formation of coherent vortex structures Simpson (1989). The dimensionless shear layer thickness is defined as $\delta_\omega = (U_{max} - U_{min})/(\partial u/\partial y)_{max}$, where U_{max} and U_{min} are the maximum and minimum mean streamwise velocities, respectively Li & Wang (2024). The shear layer thickness has been reported to grow linearly with downstream distance Agelinchaab & Tachie (2008). For low aspect ratios, the shear layer extends along the upper surface of the separation region and persists downstream until a reattachment point is established on the wall van der Kindere & Ganapathisubramani (2018). For longer obstructions, the flow separated at the leading edge reattaches along the upper surface, marking the formation of the first separation region and its associated shear layer. The free stream leaving the upper surface then convects downstream towards the trailing edge, where it overlies the wake recirculation region. This second interaction between the wake separation and the flow exiting the trailing edge establishes the second shear layer van der Kindere & Ganapathisubramani (2018).

The flow topologies described above correspond to the time-averaged flow field. Instantaneous observations of the recirculation region reveal a flapping behaviour driven by the impingement of the free stream on the separated region. This manifests as an oscillatory pattern that alters the topology of the shear layer and the instantaneous reattachment location Graziani *et al.* (2017).

The regions of high shear ($\partial u/\partial y$) that form when the flow separates are known to exhibit significant levels of fluctuating velocity components u', v', w'. These fluctuations are concentrated along the shear layer, with peak values located immediately downstream of the leading edge, where the free stream accelerates past the obstruction and impinges on the top recirculation region. At the point of separation, the shear layer is narrow, producing a sharp velocity gradient and a highly energetic region. As the flow progresses downstream, the shear layer widens and the interaction intensity decreases Larose *et al.* (2025); van der Kindere & Ganapathisubramani (2018); Cimarelli *et al.* (2018). These results confirm a direct correlation between the impinging free stream and the top-surface recirculation region. While the free-stream intensity is governed by the Reynolds number, the recirculation region properties are governed primarily by the obstruction geometry, particularly the aspect ratio, for a fixed step height. Nevertheless, for short obstructions, the returning flow has been shown to significantly affect both the topology and the flow properties of the top recirculation region.

This study examines the effect of obstruction geometry on the shear layer and the dynamics of the top recirculation region. The conventional rectangular obstruction is generalised through the introduction of a sloped trailing-edge angle α, yielding a right-angled trapezoidal geometry (Fig. 2(c)). The resulting configuration introduces a multi-parameter geometry defined by both the obstruction length L and the trailing-edge angle α, while the height h is held constant.

2 Experimental Methodology

The layout of the experimental system is shown in Figure 2(a). The test section has a square cross-section measuring 25 mm wide by 200 mm tall. The flow is driven by a 30 hp centrifugal pump, regulated via a variable frequency drive (VFD), enabling control of the free-stream velocity up to 15 $\mathrm{m\,s^{-1}}$. To prevent cavitation, the maximum operating velocity was limited to 7 $\mathrm{m\,s^{-1}}$. The working fluid was filtered water, uniformly seeded with 2 μm silver-coated glass spheres to facilitate Particle Image Velocimetry (PIV). All experiments were conducted at a Reynolds number based on the obstacle height of $Re_h = U_\infty h/\nu = 60{,}000$, where $U_\infty = 6.7\ \mathrm{m\,s^{-1}}$ is the free-stream velocity, $h = 10$ mm is the obstacle height, and ν is the kinematic viscosity of water. The estimated Stokes number of the tracer particles, based on the smallest turbulent scales, is 0.033. The boundary layer was characterised separately, yielding a thickness of $\delta_{99} \approx 10$ mm at the model location, approximately equal to the obstacle height.

A Stereo Particle Image Velocimetry (SPIV) system was employed to measure three-component velocity fields. Two LaVision Imager CX-25 cameras, each equipped with a 100 mm macro lens and a Scheimpflug adapter, were positioned downstream of the model at viewing angles of approximately 5° and 20° relative to the flow direction. Illumination was provided by a double-pulsed Nd:YAG laser (Quantel EverGreen 532-200) forming a sheet approximately 1 mm thick, oriented vertically through the central plane of the test section. Stereo image pairs were acquired at a frequency of 5 Hz and processed using DaVis 11.2 (LaVision GmbH). The key parameters of the SPIV setup are summarised in Table 1.

Experiment	**Stereo PIV**
Field of View (mm)	107×54
Frequency (Hz)	15
Vector Resolution (μm)	217
Sum-of-Correlation (μm)	54
Snapshots	3000
Run Time (s)	200
Cameras	2× Imager CX-25
Tracer Particles	2 μm silver-coated hollow glass spheres

Table 1. Parameters of the stereo PIV imaging setup used in this study.

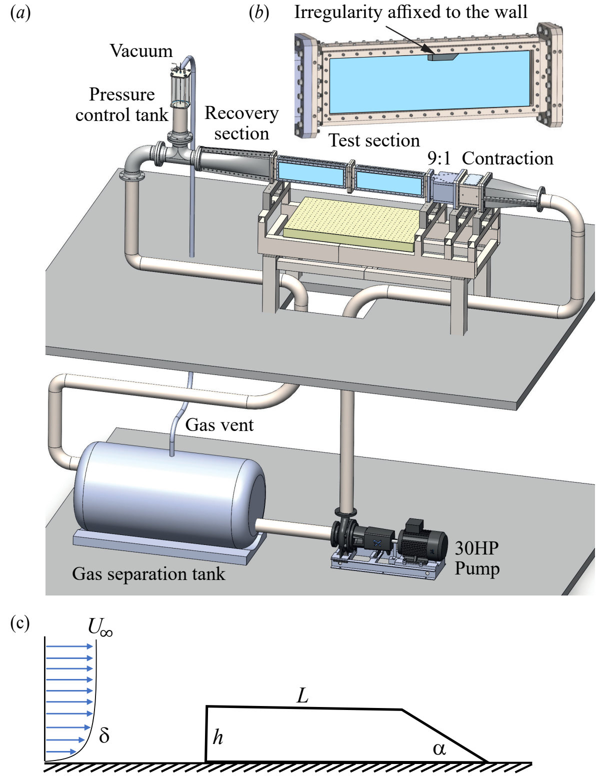

Figure 2. A schematic overview of the experimental setup. The closed-loop water tunnel constructed at the Technion Transient Fluid Mechanics Laboratory.

3 Results

3.1 Effects of geometry on the mean separated flow

Figure 3 presents the experimentally obtained streamwise velocity fields in the vicinity of the top-surface and wake separation regions for $L^* = 1,4$ and $\alpha = 30°, 90°$. The colour scale is defined such that yellow and red indicate forward flow ($u > 0$), while blue denotes reverse flow ($u < 0$). A consistent pattern is observed across all recirculation regions: the forward and return flows within the recirculating region are separated by a narrow white band corresponding to the approximate stagnation contour ($u \approx 0$). The upstream separation, which is governed primarily by the Reynolds number and the incoming boundary layer thickness, remains largely invariant across all tested aspect ratios and has a negligible influence on the top-surface and wake flow characteristics. It is therefore not discussed further here. The present results are in good agreement with previous studies, confirming the established separation topologies for varying obstruction lengths.

The general behaviour of the separated flow is consistent with previous measurements for obstruction lengths that do not exceed $L/h = L^* < 3.5$ van der Kindere & Ganapathisubramani (2018). For short protrusion lengths (*a,b*), the flow exhibits a clear pattern of interaction between the leading-edge and wake regions. A streamline originating near the reattachment point follows the foot of the obstruction along its back face and extends towards the leading-edge separation point. This indicates that fluid is recirculating along the entire perimeter of the separation region. In contrast, for the longer obstruction (*c,d*) with $L^* = 4$, the coupling between the top-surface and wake regions vanishes. The previously unified recirculation restructures into two distinct recirculation zones, originating independently at the leading edge and in the obstruction wake. Both top-surface regions (*c,d*) exhibit similar spatial extents and reattachment locations. The influence of reverse flow remains evident, but is reduced in scale and confined within each individual region. Flow in the wake region convects exclusively in the downstream direction, leaving the top-surface recirculation effectively independent.

For the case of the sloped trailing edge ($\alpha = 30°$) at $L^* = 4$ (*d*), separation is delayed relative to the right-angle case and initiates along the curved back face of the obstruction rather than at the trailing edge. The resulting recirculation region is spatially reduced compared to its right-angle counterpart (*c*), suggesting a narrower buffer between the separated flow and the free stream and thus a weaker shear-layer effect.

Both trailing-edge angles exhibit the same general trend of reversed streamlines along the back face of the obstruction. However, the sloped trailing edge ($\alpha = 30°$) produces a gradual, smooth flow ascent along the surface, whereas the right-angle geometry imposes an abrupt change in surface direction. In the latter case, the streamlines are unable to follow the sharp corner, resulting in an internal recirculation region. The forward flow within this recirculation is nonetheless substantially weaker than in the free stream. Across all tested geometries,

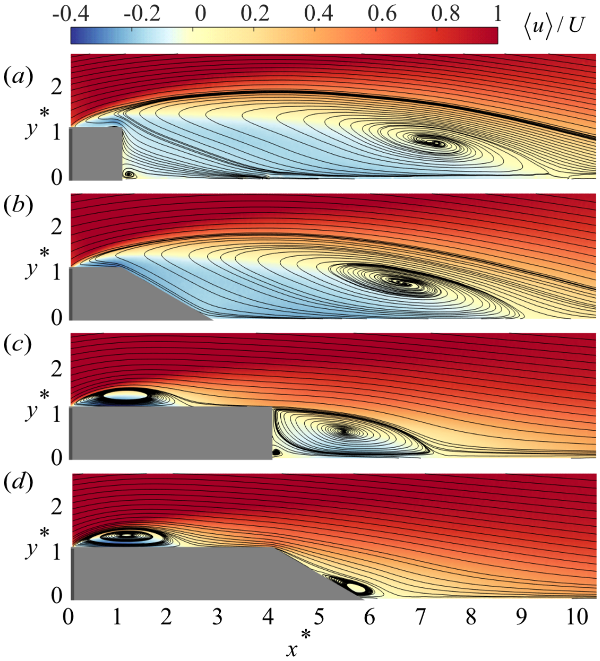

Figure 3. Comparison of trailing-edge angles $\alpha = 30°$ and $90°$ for obstruction lengths $L^* = 1$ and 4: *(a)* $L^* = 1$, $90°$; *(b)* $L^* = 1$, $30°$; *(c)* $L^* = 4$, $90°$; *(d)* $L^* = 4$, $30°$.

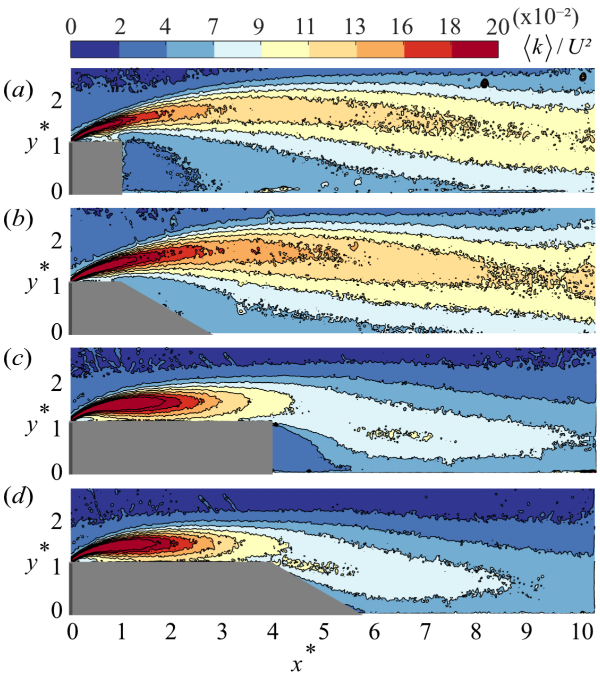

Figure 4. Comparison of turbulent kinetic energy for trailing-edge angles $\alpha = 30°$ and $90°$ at obstruction lengths $L^* = 1$ and 4: *(a)* $L^* = 1$, $90°$; *(b)* $L^* = 1$, $30°$; *(c)* $L^* = 4$, $90°$; *(d)* $L^* = 4$, $30°$.

regions of dense streamline concentration are indicative of pronounced velocity gradients and are associated with enhanced mixing, primarily at the interface between the free stream and the shear layer.

3.2 Effects of geometry on turbulent kinetic energy

Figure 4 presents the experimentally obtained turbulent kinetic energy (TKE) distributions for obstruction lengths $L^* = 1$ and 4 at trailing-edge angles $\alpha = 30°$ and $90°$. The contour levels are distributed uniformly across 10 discrete levels in the range $TKE/U_\infty^2 \in [0, 20] \times 10^{-2}$.

For the short models ($L^* = 1$) with both right-angle and sloped trailing edges (*a,b*), the shear layer extends to more than10 obstacle heights downstream. The peak TKE reaches $\langle k \rangle / U_\infty^2 \approx 20 \times 10^{-2}$ and is located immediately downstream of the leading edge, where the high-intensity shear layer is thinnest. Beyond this peak, the TKE magnitude decays monotonically in the downstream direction while the contours expand spatially in a conical pattern. The subsequent contour levels, $TKE/U_\infty^2 \in \{9\text{–}11, 7\text{–}9, 4\text{–}7\} \times 10^{-2}$, continue to develop in the same conical fashion, with their full streamwise extent lying beyond the field of view.

For the long models ($L^* = 4$) with both right-angle and sloped trailing edges (*c,d*), two distinct recirculation regions are observed: one on the top surface of the obstruction, where the first reattachment point occurs, and one in the wake. At this aspect ratio, the trailing-edge angle has no significant influence on the top-surface separation region, and consequently the first three TKE contour levels remain largely unchanged in both magnitude and spatial distribution between the two geometries. The secondary wake separation is characterised by a substantial momentum deficit in both configurations, and the associated TKE distribution is less intense and spatially smoother than its top-surface counterpart. A clear distinction is nonetheless observed in the location of the local TKE peak, $\langle k \rangle / U_\infty^2 \in [9, 11] \times 10^{-2}$: for the right-angle case ($\alpha = 90°$), this peak is located at the trailing edge, whereas for the sloped configuration ($\alpha = 30°$) it shifts downstream to the shear-layer interface between the free stream and the wake recirculation region.

Tables 2 and 3 quantify the streamwise extent of the TKE contours for each trailing-edge angle. The results show that, for short obstruction lengths, the streamwise extension of the elevated TKE region is considerably more pronounced for the sloped trailing edge.

$\lvert k \rvert \cdot 10^{-2}$	$L^* = 1$, $\alpha = 90°$	$L^* = 1$, $\alpha = 30°$	**Relative elongation**
[18, 20] ●	1.0	1.3	30 % increase
[16, 18] ●	1.3	1.9	46 % increase
[13, 16] ●	2.9	5.0	72 % increase

Table 2. Streamwise extent of TKE contour levels quantified from Figure 4 (*a,b*).

$\lvert k \rvert \cdot 10^{-2}$	$L^* = 4$, $\alpha = 90°$	$L^* = 4$, $\alpha = 30°$	**Relative elongation**
[18, 20] ●	1.9	1.7	90 % decrease
[16, 18] ●	2.2	2.1	95 % decrease
[13, 16] ●	2.6	2.5	96 % decrease

Table 3. Streamwise extent of TKE contour levels quantified from Figure 4 (*c,d*).

Conclusion

This study examines the effect of the returning flow on separation dynamics induced by a surface-mounted trapezoidal obstruction with a sloped trailing edge. The influence of varying trailing-edge angles on the resulting flow topology is investigated, with particular attention to the velocity field, the formation and extent of separation regions, the spatial distribution of the shear layer, and the consequent TKE intensity in the vicinity of the obstruction.

The effect of the sloped trailing edge is shown to be most pronounced for short aspect ratio models. The observed increase in TKE intensity is attributed to the elevated momentum carried by the returning flow as it ascends along the curved back face of the obstruction. This returning flow, carrying elevated streamwise momentum, impinges on the top surface and interacts with the incoming free stream, producing an amplified collision that drives intense turbulent activity and increased TKE.

For long obstructions, however, this effect diminishes: the observed TKE, in both magnitude and spatial distribution, shows negligible differences between the right-angle and sloped configurations. The influence of the trailing-edge geometry on TKE is therefore bounded by the obstruction aspect ratio.

REFERENCES

Agarwal, Karuna, Ram, Omri, Lu, Yuhui & Katz, Joseph 2023 On the pressure field, nuclei dynamics and their relation to cavitation inception in a turbulent shear layer. *Journal of Fluid Mechanics* **966**, A31.

Agelinchaab, Martin & Tachie, Mark F 2008 Piv study of separated and reattached open channel flow over surface mounted blocks. *Journal of Fluid Engineering* .

Agyei-Agyemang, Kwasi Hyiah, Essel, Ebenezer E & Tachie, Mark F 2024 Effects of aspect ratio on flow characteristics on free surface-mounted rectangular cylinders. *International Journal of Heat and Fluid Flow* **109**, 109535.

Chen, Lin, Asai, Keisuke, Nonomura, Taku, Xi, Guannan & Liu, Tianshu 2018 A review of backward-facing step (bfs) flow mechanisms, heat transfer and control. *Thermal Science and Engineering Progress* **6**, 194–216.

Cimarelli, Andrea, Leonforte, Adriano & Angeli, Diego 2018 On the structure of the self-sustaining cycle in separating and reattaching flows. *Journal of Fluid Mechanics* **857**, 907–936.

Fang, Xingjun, Tachie, Mark F & Dow, Karen 2022 Turbulent separations beneath semi-submerged bluff bodies with smooth and rough undersurfaces. *Journal of Fluid Mechanics* **947**, A19.

Graziani, A., Lippert, M., Uystepruyst, D. & Keirsbulck, L. 2017 Scaling and flow dependencies over forward-facing steps. *International Journal of Heat and Fluid Flow* **67**, 220–229.

Hattori, Hirofumi & Nagano, Yasutaka 2010 Investigation of turbulent boundary layer over forward-facing step via direct numerical simulation. *International Journal of Heat and Fluid Flow* **31** (3), 284–294, sixth International Symposium on Turbulence and Shear Flow Phenomena.

Kostas, J, Soria, Julio & Chong, M 2002 Particle image velocimetry measurements of a backward-facing step flow. *Experiments in fluids* **33** (6), 838–853.

Larose, Emil, Kerhervé, Franck, Fraigneau, Yann, Podvin, Bérengère, Morton, Chris & Martinuzzi, Robert J. 2025 Effects of oncoming flow conditions on the flow upstream of a forward-facing step subject to a thin boundary layer. *International Journal of Heat and Fluid Flow* **115**, 109866.

Li, Sicheng & Wang, Jinjun 2024 Entrainment of the shear layer separated from a wall-mounted fence. *Journal of Fluid Mechanics* **999**, A6.

Pastoor, Mark, Henning, Lars, Noack, Bernd R, King, Rudibert & Tadmor, Gilead 2008 Feedback shear layer control for bluff body drag reduction. *Journal of Fluid Mechanics* **608**, 161–196.

Sagharichi, Amir, Aleyasin, Seyed Sobhan & Tachie, Mark Francis 2023 Turbulent separations around a slanted-back ahmed body with square and rounded leading edge. *Physics of Fluids* **35** (4).

Scharnowski, Sven, Bolgar, Istvan & Kähler, Christian J 2017 Characterization of turbulent structures in a transonic backward-facing step flow. *Flow, Turbulence and Combustion* **98** (4), 947–967.

Scheit, C., Esmaeili, A. & Becker, S. 2013 Direct numerical simulation of flow over a forward-facing step – flow structure and aeroacoustic source regions. *International Journal of Heat and Fluid Flow* **43**, 184–193, 7th International Symposium on Turbulence Heat & Mass Transfer (THMT-7), Palermo Conference on Modelling Fluid Flow (CMFF'12).

Schröder, Andreas, Willert, Chris, Schanz, Daniel, Geisler, Reinhard, Jahn, Tobias, Gallas, Quentin & Leclaire, Benjamin 2020 The flow around a surface mounted cube: a characterization by time-resolved piv, 3d shake-the-box and lbm simulation. *Experiments in Fluids* **61** (9), 189.

Simpson, Roger L 1989 Turbulent boundary-layer separation. *Annual Review of Fluid Mechanics* **21** (1), 205–232.

van der Kindere, J. & Ganapathisubramani, B. 2018 Effect of length of two-dimensional obstacles on characteristics of separation and reattachment. *Journal of Wind Engineering and Industrial Aerodynamics* **178**, 38–48.

Yamada, S & Nakamura, H 2016 Construction of 2d-3c piv and high-speed infrared thermography combined system for simultaneous measurement of flow and thermal fluctuations over a backward facing step. *International Journal of Heat and Fluid Flow* **61**, 174–182.